Giant Anomalous Ettingshausen effect and Hybrid longitudinal-transverse thermoelectric Cooling in a Nanoscale Magnetic Weyl Semimetal

Mohammadali Razeghi,[†] Jean Spiece,[†] Valentin Fonck,[†] Yao Zhang,[‡,¶] Michael Rohde,[†] Rikkie Joris,[§] Phillip S. Dobson,[‖] Jonathan M. R. Weaver,[‖] Lino M. C. Pereira,[§] Simon Granville,[‡,¶] and Pascal Gehring[*,†,⊥]

†*Institute of Condensed Matter and Nanosciences, Université catholique de Louvain (UCLouvain), Louvain-la-Neuve, 1348, Belgium*

‡*Robinson Research Institute, Victoria University of Wellington, Wellington, 6140, New Zealand*

¶*The MacDiarmid Institute for Advanced Materials and Nanotechnology, Wellington, 6011, New Zealand*

§*Quantum Solid State Physics, KU Leuven, Leuven, 3001, Belgium*

‖*James Watt School of Engineering, University of Glasgow, Glasgow, G12 8LT, United Kingdom*

⊥*WEL Research Institute, Avenue Pasteur 6, Wavre, 1300, Belgium*

E-mail: pascal.gehring@uclouvain.be

Abstract

Solid-state cooling devices offer compact, quiet, reliable and environment-friendly solutions that currently rely on conventional thermoelectric (TE) effects. Despite more than two centuries of research, classical thermoelectric coolers suffer from low efficiency which hampers wider application. In this study, a combination of the less researched Anomalous Ettingshausen effect (AEE), a transverse thermoelectric phenomenon, and a geometrically induced Peltier effect is presented as an approach for on-chip cooling. The anomalous Ettingshausen effect can be boosted in materials with non-trivial band topologies as demonstrated in the Heusler alloy Co_2MnGa. Enabled by the high quality of our material, in situ scanning thermal microscopy experiments reveal a giant anomalous Ettingshausen coefficient of 3.1 mV in µm-sized on-chip cooling devices at room temperature. A significant 57% of the effect is contributed by the intrinsic topological properties, in particular the Berry curvature of Co_2MnGa. We then demonstrate that a geometrical Peltier effect can be induced in the films by fabricating nano-ribbon devices which increases the figure of merit by 170%. The combined cooling action of the anomalous Ettingshausen and the Peltier effect yield a nm-sized local spot cooler emphasising the potential of nano-structured magnetic Weyl semimetals.

Keywords: Anomalous Ettingshausen effect, Magnetic Weyl semimetals, topology, Peltier effect, SThM, on-chip spot-cooling.

Introduction

The constraints that typically limit the efficiency of conventional thermoelectric materials where heat and charge flow in parallel do not apply to the Ettingshausen effect (EE, see Figure 1a), a *transverse* thermoelectric phenomenon similar to the Hall effect, where heat and charge currents are orthogonal. When a charge current density $\mathbf{j}_c$ flows through a material exposed to a magnetic field $\mathbf{B}$, a heat current density $\mathbf{j}_{q,EE}$ is generated perpendicularly to both (see Figure 1a and Figure S2 for more details about how the directions of charge and heat currents are defined in this manuscript).

Thanks to their orthogonality, heat and charge flow are decoupled, which eliminates

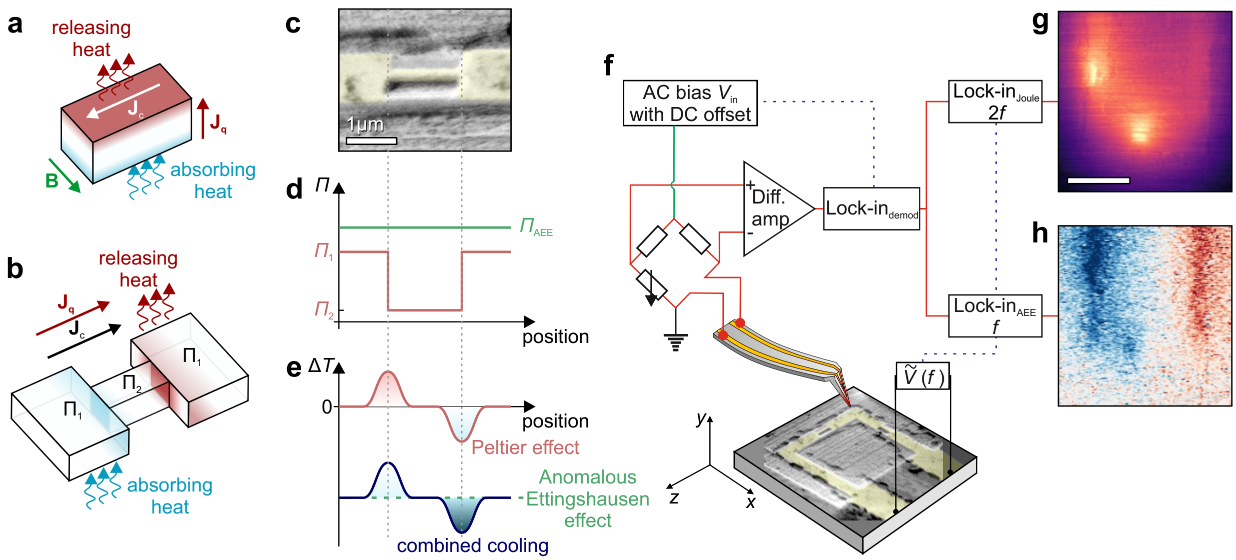

Figure 1: **Combined Ettingshausen and Peltier cooling in nanoscale junctions.** **a,** The charge current $\mathbf{J}_{\mathrm{c}}$, defined as a current flowing from positive to negative terminal of voltage source, passes through an Ettingshausen cooler which is exposed to a magnetic field $\mathbf{B}$. This induces a transverse heat flux $\mathbf{J}_{\mathrm{q}}$, which decreases/increases the bottom/top surface temperature, thereby establishing a temperature gradient ∇T from cold to hot, i.e., $\nabla T || \mathbf{J}_{\mathrm{q}}$. **b,** A geometrically induced thermocouple is formed between narrow (Π_2) and wide (Π_1) regions of a material. Passing J_{c} through the junctions absorbs/releases Peltier heat from/at the interface. **c,** False-color SEM image showing a Co_2MnGa (yellow) film which was patterned into a nanoribbon (borders of nanoribbon are outlined by dashed lines). **d,** Change of the Peltier (red) and anomalous Ettingshausen coefficient along the nanoribbon device in (c). **e,** Temperature change along the nanoribbon device. Heating/cooling is expected at the two Peltier junctions (red line). When a magnetic field is applied, the Anomalous Ettingshausen effect (AEE) adds a constant cooling background (green dotted line). This leads to combined action of Peltier and anomalous Ettingshausen cooling (blue curve). **f,** An AC current J_{c} is injected into the U-shape Co_2MnGa device (SEM micrograph shown) using an AC voltage bias $\widetilde{V}$ at frequency f (black lines). The SThM tip is biased with a small AC and DC offset (V_{in}, green line) using a Wheatstone bridge. A first lock-in demodulates the signal with respect to the tip excitation. Subsequently, a second lock-in demodulates the second ($2 \times f$) and first harmonic (f) corresponding to the Joule (**g**) and AEE/Peltier (**h**) response, respectively (scale bar: 10 μm). These signals are further converted into temperature variation maps via tip calibration (see methods and Supporting Information section 1).

Joule heating's parasitic contributions, significantly boosting conversion efficiency. Consequently, Ettingshausen coolers hold the record for the lowest temperature achieved by room temperature thermoelectric cooling.[1] However, the Ettingshausen effect typically requires a substantial external magnetic field, often several Tesla, to operate. Recent research has shown that this hurdle can be overcome by leveraging materials with nontrivial band topologies. Akin to the anomalous Hall effect, the thermoelectric counterparts, the anomalous Nernst/Ettingshausen effects, depend on the magnetization of the compound and on the anomalous velocity of electrons linked to the band structure's Berry curvature which can be significant in magnetic materials. Remarkably, a class of quantum materials known as magnetic Weyl semimetals boasts exceptionally large[2] (or even 'giant'[3]) anomalous Nernst coefficients due to their topologically non-trivial band structure. This discovery could unlock the high-performance spot cooling potential, as the anomalous Nernst and Ettingshausen coefficients are closely linked through the Bridgman relation.[4] Nonetheless, precise measurement of cooling effects in nanostructures remains challenging due to limitations in instrumentation or material quality,[5] and experimental evidence for such significant Ettingshausen cooling efficiency awaits confirmation.

Here, we find a giant room-temperature anomalous Ettingshausen coefficient in the Heusler alloy Co_2MnGa. To further boost the cooling power and enable local spot-cooling devices with nm-sized footprint, we fabricated Co_2MnGa nanoribbon devices where a local Peltier effect is geometrically induced (see Figure 1b). We then performed frequency- and magnetic field-dependent local thermometry and local thermal transport experiments by means of Scanning Thermal Microscopy (SThM). Our findings reveal the important contribution of topology to the transverse thermoelectric effect in our samples and show that the total cooling power can be doubled by geometrically induced Peltier effects. This demonstrates that nanoscale anomalous Ettingshausen devices are strong candidates for on-chip cooling applications.

Results

High-quality single-crystalline, epitaxial Co_2MnGa thin films with a thickness of 50 nm were deposited on single-crystalline MgO (001) substrates by DC magnetron sputtering. As previously demonstrated through detailed structural characterization involving XRD θ–2θ scans and ϕ-scans, our Co_2MnGa film exhibits four-fold symmetry, confirming the epitaxial relationship MgO(001)[100] ∥ Co_2MnGa(001)[110] and rotated cube-on-cube growth.[6] The Co_2MnGa films are capped by a thin Ta layer to prevent oxidation (see Methods for details). Since the heat current density $\mathbf{j}_{\mathrm{q,AEE}}$ generated by the anomalous Ettingshausen effect (AEE) depends on the direction of the charge current density $\mathbf{j}_c$ and the magnetization $\mathbf{M}$ (unit vector $\mathbf{m}$), it can be written as[7,8]

$$\mathbf{j}_{\mathrm{q,AEE}} = \Pi_{\mathrm{AEE}} \cdot (\mathbf{j}_c \times \mathbf{m}) \,, \tag{1}$$

where the proportionality constant Π_{AEE} is the anomalous Ettingshausen coefficient. We patterned the Co_2MnGa thin films into microscale U-shaped devices (see Methods). This allows parallel and perpendicular $\mathbf{m}$ and $\mathbf{j}_c$ to be realised in a single device, leading to areas without ($\mathbf{j}_c \times \mathbf{m} = 0$), and with positive ($\mathbf{j}_c \times \mathbf{m} > 0$) or negative ($\mathbf{j}_c \times \mathbf{m} < 0$) Ettingshausen response, respectively. This geometry further allows differentiation between the Ettingshausen effect and other thermoelectric effects like the magneto-Peltier effect[9,10] (see Supporting Information Figure S4). To further locally boost the cooling efficiency of the Co_2MnGa device, we introduced local Peltier junctions by reducing the width of the leg and forming a nanoribbon (Figure 1c). This geometric constraint shortens the electron mean free path l_{mfp}, which can effectively modify the Peltier coefficient (Figure 1d).[11,12] This effect is strongest when the ribbon width w is smaller than l_{mfp}. As a result, the junction locally experiences cooling/heating when a charge current passes through the interface between the micro- and the nano-scale Co_2MnGa ribbon with Peltier coefficients Π_1 and Π_2, respectively:

$$\mathbf{j}_{\mathrm{q,Peltier}} = (\Pi_1 - \Pi_2) \cdot \mathbf{j_c}. \tag{2}$$

This local Peltier effect can add up to the anomalous Ettingshausen effect and lead to locally enhanced cooling performance (Figure 1e).

To measure the local temperature distribution on Co_2MnGa on-chip coolers with nanometer spatial and mK temperature resolution, we employed an AC-SThM method[12–14] (see Figure 1f). To this end, the Co_2MnGa U-shaped device is biased by a sinusoidal alternating current (AC) with frequency f and amplitude J_c. Joule and Ettingshausen/Peltier temperatures can then be obtained by demodulating the thermometer signal of the SThM probe at $2f$ and f, respectively. To study the anomalous Ettingshausen cooling without Peltier contribution, we first examined a device with a constant channel width of 1 µm where no geometrically induced Peltier effect is expected. Joule and AEE temperature maps recorded at a charge current $J_c = 0.95$ mA, $f = 17$ Hz, and in-plane magnetic field of 80 mT are shown in Figure 1g,h. While Joule heating raises the temperature of the three sides of the U-shaped device equally, the Ettingshausen effect increases (decreases) the temperature in areas where the magnetic field is perpendicular to the current. For areas where the magnetic field is parallel to the charge current, no temperature change is observed, in accordance with Eq. 1. The direction of $\mathbf{j}_q$ with respect to $\mathbf{j}_c$ and B in such experiments was further confirmed by additional AC+DC experiments as described in Section 1 and Figure S2 of the Supporting Information.

In Figure 2, we further investigate the magnetic-field dependence of the AEE effect. Figures 2a, c, e and b, d, f show the Joule and AEE response, respectively, at -80 mT, 0 mT, and 80 mT. We observe AEE maps of similar spatial distribution and amplitude but with opposite signs for -80 mT and 80 mT as expected from Eq. 1. For $\mathbf{B} = 0$, no AEE signal is observed within our experimental resolution limit. The Joule heating maps (Figures. 2a,c,e) are not affected by the magnetic field. To further investigate the influence of current density, magnetic field and frequency, we placed the SThM probe at a constant location on the right leg of the U-shaped device. The force between the probe and the sample is kept constant using the AFM feedback loop. Figure 2g illustrates the linear correlation between the T_{AEE} and the applied current density $\mathbf{j}_c$, as expected from Eq. 1, with $\mathrm{d}T_{\mathrm{AEE}}/\mathrm{d}j_c = 1.8 \times 10^{-12}$ $\mathrm{m^2KA^{-1}}$, while a quadratic response is observed in Joule heating (see Supporting Information

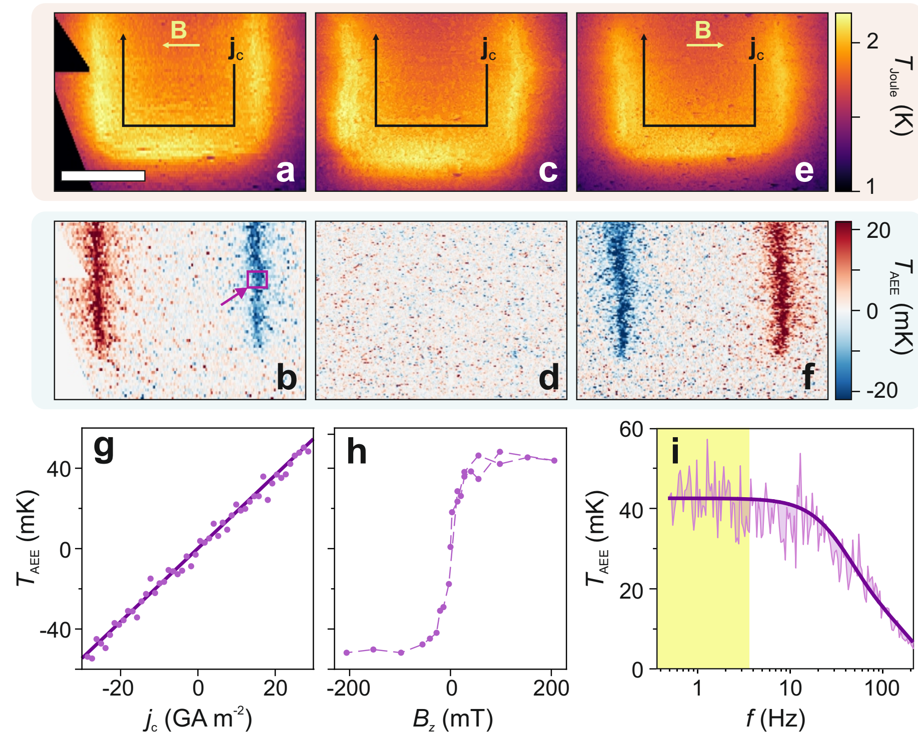

Figure 2: **Anomalous Ettingshausen effect and Joule heating in Co_2MnGa. a,c,e,** Maps of T_{Joule} and **b,d,f,** T_{AEE} for the U-shaped 50-nm-thick Co_2MnGa film, measured at a frequency of f=17 Hz, current density $j_c = 19$ GA m^{-2} (current $J_c = 0.95$ mA) and under a magnetic field B_z of -80 mT (**a,b**), 0 (**c,d**), and 80 mT (**e,f**). **g,** T_{AEE} as a function of charge current density j_c measured on the right leg (see purple square highlighted by arrow) at $B_z = 80$ mT and $f = 17$ Hz. Solid line: linear fit to the data. **h,** T_{AEE} as a function of magnetic field B_z at $j_c = 28.5$ GA m^{-2} and $f = 17$ Hz. **i,** T_{AEE} as a function of frequency f measured at $j_c = 19$ GA m^{-2} and $B_z = 80$ mT. Scale bar: 10 µm. The black/white triangles in (a) and (b) are artifacts from correcting the drift of our microscope.

Figure S5). Figure 2h shows the magnetic field dependence of the T_{AEE}. We observe a steep increase of the signal at low fields, followed by saturation at a field of $B \approx 50$ mT, which qualitatively follows the magnetization of our films measured by volumetric magnetometry (see Supporting Information Figure S9c). Such saturation is the hallmark of an anomalous Ettingshausen effect, and the anomalous Ettingshausen coefficient can be extracted from this saturation region. Lastly, we observe that T_{AEE} decreases with increasing AC frequency of J_c (Figure 2i). This reflects the thermal response time of the system (the U-shaped device and substrate), which is on the order of 30 ms, as obtained by fitting a RC low-pass model (solid curve in Figure 2i). Conversely, at low frequencies, the signal maximizes and approaches the steady-state value used to quantify Π_{AEE}.

It is worth mentioning that the spatial temperature distribution in the Joule and AEE maps differs noticeably. As shown in the Supporting Information Figure S8, while Joule heating decays over several µm around the U pattern, the AEE signal is localized around the device. This distinction highlights the differing origins of the generated heat: whereas Joule heating is produced uniformly and isotropically throughout the entire film, the AEE heat current is directional, flowing from the heat source to a heat sink positioned along the top and bottom sides of the device.[15] This confined temperature distribution created by the AEE allows for precise local temperature control that cannot be achieved using conventional methods that have high thermal diffusion.

In the following, we study the geometrically induced Peltier effect and the impact of nanostructuring on the AEE coefficient in Co_2MnGa nanoribbon devices using SThM (Figure 3). To this end, we systematically vary the Co_2MnGa ribbon width from 4.2 µm down to 450 nm. The device, shown in Figure 3a, features five different ribbon widths. Unlike the uniform temperature distribution along the parallel legs of the U-shaped structure in Figure 2b,f, altering the ribbon width significantly affects the AEE signal, with narrower sections exhibiting a stronger AEE response. Since the same current J_c flows through all sections during temperature mapping, the current density j_c is higher in the narrower regions, leading to an increase in AEE heat current, as expected from Eq. 1. Thus, to compare the cooling effect across different widths, we computed the corresponding Π_{AEE} from the measured T_{AEE}. Using Eq. 1, it is possible to derive an expression for Π_{AEE} given by experimentally accessible parameters. Considering T_{AEE} in steady state regime, Π_{AEE} can be expressed as:[8,9,16]

$$\Pi_{\mathrm{AEE}} = \frac{\kappa \cdot 2T_{\mathrm{AEE}}}{j_c \cdot L}, \tag{3}$$

where κ is the thermal conductivity and L is the thickness of the film. We measured the

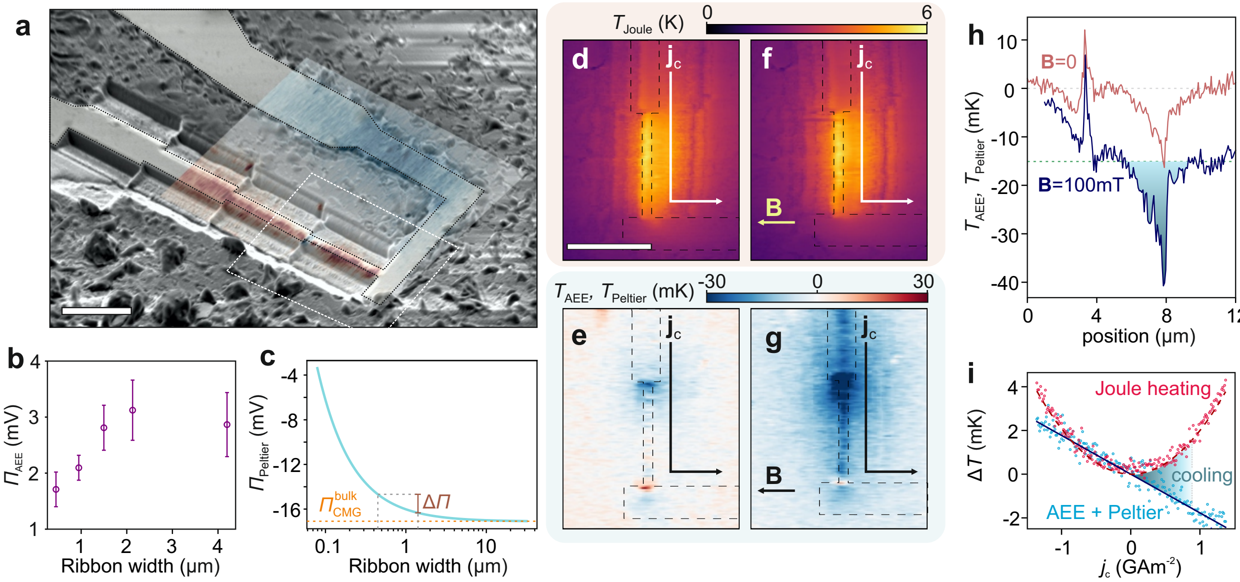

Figure 3: **Geometrically induced local Peltier effect**. **a** False-colour SEM image of a U-shaped device where the width of the channel is altered. Scale bar is 5 μm. **b**, Width dependence of the experimental anomalous Ettingshausen coefficient of Co_2MnGa nanoribbons. **c**, Evolution of the effective Peltier coefficient as a function of ribbon width for a 50 nm thick Co_2MnGa film using Eq. 4. The extended thin-film value is shown by the dotted orange line. Forming a junction between a wide (1.5 μm) and a narrow (450 nm) ribbon leads to a geometrically induced change in Peltier coefficient $\Delta\Pi$. **d,f**, Joule and **e,g**, Peltier/Ettingshausen images of the narrowest nanoribbon (the position of the nanoribbon is indicated by the dashed white square in panel (a)) at zero magnetic field (**d,e**) and at an in-plane magnetic field of 80 mT (**f,g**). **h**, Line-cuts of the data shown in **e,g** along the nanoribbon device. Scale bar: 5 μm. **i** Joule heating and Peltier/AEE cooling as a function of current density j_c, measured on the junction formed between the narrow and the wider ribbon. Cooling dominates Joule heating up to a current density of 1 GAm^{-2}, indicated by the blue shaded area. The noise floor is 0.35 mK for $T_{AEE+Peltier}$ and 0.25 mK for T_{Joule}.

thermal conductivity, κ, using SThM (see Supporting Information Section 8) and obtained a value of 22 ± 4 W K^{-1} m^{-1}, which remained constant across different nanoribbon widths. For each width, T_{AEE} was determined by spatially averaging the T_{AEE} map over regions containing at least 20 pixels. A factor of 2 was applied to account for the temperature difference between the top and bottom surfaces of the sample. The root-mean-square (RMS) of these spatially averaged T_{AEE} values, together with the systematic uncertainty from κ, was propagated through the calculation of Π_{AEE} and is represented as error bars in Figure 3b. We obtained $\Pi_{AEE} = 3.1 \pm 0.5$ mV for a ribbon width of 1.5 μm. As can be seen in Figure 3b,

Π_{AEE} decreases when reducing the ribbon width, with a noticeable drop for widths below 1 µm. The deviation from the bulk value in narrow ribbons may be attributed to a reduction in the Berry curvature contribution to the anomalous Ettingshausen effect as the channel width is reduced. Similar geometry-dependent behavior has been previously observed for the thickness dependence of the anomalous Hall effect[6] and the anomalous Nernst coefficient[2] in Co_2MnGa thin films. In the former case, the reduction in anomalous behavior is linked to the suppression of the Berry curvature contribution from majority spins with decreasing film thickness, and in sufficiently thin samples, extrinsic mechanisms, particularly side-jump scattering, dominate the magnetotransport response.[6] Furthermore, the recently discovered current-induced nonlinearity in Co_2MnGa magnetoresistance, which intensifies in narrow ribbons, may reduce Π_{AEE}. The applied current, along with the resulting Joule heating, establishes a temperature gradient toward the substrate, generating a transverse thermoelectric field along the ribbon. The resulting counteracting charge current reduces J_c and may further contribute to the deviation of the measured anomalous Ettingshausen coefficient from its bulk value.[17] This finding is crucial for the design of future optimized micro-cooler devices, suggesting that to maximize the AEE effect, the spot cooler dimensions should be kept above 1 µm. The values we measured for Π_{AEE} agree well with the value 2.3 mV estimated using the Bridgman relation $\Pi_{\mathrm{AEE}} = S_{\mathrm{ANE}} \cdot T$ and the experimental anomalous Nernst coefficient of our films.[18] Both positive[19,20] and negative[2,18,21,22] values have been reported for the anomalous Nernst coefficient of Co_2MnGa due to the use of different conventions: the thermoelectric and the vortex conventions explained in Behnia.[23] In the vortex convention, originating from studies of the vortex Nernst effect, a positive Nernst coefficient corresponds to a transverse voltage generated by the motion of superconducting vortices from hot to cold in a magnetic field. In contrast, the thermoelectric convention defines a positive Nernst signal as the emergence of an electric field along the y-axis when a thermal gradient is applied along the x-axis and a magnetic field along the z-axis, independent of vortex motion. In this work, we follow the thermoelectric convention (Figure 1a), which yields a positive Nernst-Ettingshausen effect and a positive thermoelectric tensor coefficient in Co_2MnGa. Note that adopting the vortex convention would result in the opposite sign. A schematic in Supporting Information Figure S3 illustrates the relationship between the Nernst-Ettingshausen sign definitions in both conventions.

To study the geometrically induced local Peltier effect, we recorded $2f$ (Figure 3d) and $1f$ (Figure 3e) SThM maps of a 450 nm wide Co_2MnGa nanoribbon connected to 1.5 µm wide Co_2MnGa leads at zero magnetic field. We observed local Joule heating of the nanoribbon as a result of an enhanced charge current density. Furthermore, we find local Peltier cooling and heating at the junctions between the wide Co_2MnGa regions and the nanoribbon, respectively (see red curve in Figure 3h for a linecut along the device). We attribute this to a change in Peltier coefficient (see Figures 1b and e), similar to results obtained in gold[11] and graphene[12] nanoconstrictions. Using the Fuchs-Sondheimer model and the Mott relation, the change in Peltier coefficient of a thin-film device with changing width d is

$$\Pi_{\text{Peltier}} = \Pi_{\text{CMG}}^{\text{bulk}} \left[1 - \frac{3}{8} \frac{(1-P) l_{\text{mfp}}}{w} \frac{U}{1+U} \right]. \tag{4}$$

Here $U = \left. \frac{\partial \ln l_{\text{mfp}}}{\partial \ln E} \right|_{E_F}$, P is the scattering coefficient and $\Pi_{\text{CMG}}^{\text{bulk}}$ is the Peltier coefficient of the infinitely wide Co_2MnGa film. Assuming purely inelastic scattering ($P = 0$) and using $U \to \infty$, which gives a lower bound of the electron mean free path l_{mfp}, we could fit the local Seebeck coefficient variations measured on the same junction (see SI for details) and obtained $l_{\text{mfp}} > 170$ nm. Using these values and Eq. 4 allows us to estimate the change in Peltier coefficient as a function of nanoribbon width (see Figure 3c). For the junction from 450 nm to 1.5 µm, we find $\Delta\Pi = 1.7$ mV. In Figure 3f and g, we repeat the experiment on the Co_2MnGa nanoribbon device under an in-plane magnetic field of 80 mT. Although the local Joule heating (Figure 3f) is nearly unaffected by the magnetic field, a constant anomalous Ettingshausen cooling is superimposed on the local Peltier effect (see Figure 3g and blue line cut in panel h). We find that the combination of anomalous Ettingshausen and Peltier effects locally enhances the cooling by a factor of 1.66, which, given that thermoelectric figure of merit is proportional to Π^2, would lead to an enhancement of 170% of figure of merit. Similar results were obtained for another nanoribbon device (see detailed analysis in Supporting Information Section 4).

Finally, the net harmonic cooling of the device was measured at the geometrical junction, where both Ettingshausen and Peltier cooling are present and contribute with the same sign. We found that the cooling spot radius at the junction is of the order of a few micrometers, as Peltier cooling weakens with increasing distance from the junction. A current sweep was performed while the SThM sensor measured the combined cooling at the 1st harmonic and Joule heating at the 2nd harmonic (Figure 3i). This measurement shows the active cooling range of the spot cooler – the shaded region in Figure 3i – where the combined cooling effect dominates Joule heating. As current density increases further, Ettingshausen/Peltier cooling scales linearly, while Joule heating grows quadratically, ultimately reducing the net cooling effect and causing the junction to heat up. By adding the Joule heating contribution to the combined AEE and Peltier cooling, we find a maximum cooling of $\Delta T = -0.4$ mK.

Discussion

In Figure 4a, we compare Π_{AEE} of Co_2MnGa (red star) to values reported in the literature (circles) as a function of the saturation magnetization M_{sat} of the materials.

We find, consistent with previous reports on anomalous transport coefficients,[9,16,20,25] that Π_{AEE} of Co_2MnGa does not scale with saturation magnetization values (trivial scaling indicated by the gray-shaded area). This suggests the involvement of intrinsic material properties, such as a large Berry curvature resulting from the non-trivial band topology.

To identify the origin of the large Π_{AEE} observed in Co_2MnGa, we decompose the total effect into intrinsic and extrinsic contributions. The charge current density generated by an applied electric field $\mathbf{E}$ and temperature gradient ∇T is expressed as $\mathbf{j}_{\mathrm{c}} = \boldsymbol{\sigma}\mathbf{E} - \boldsymbol{\alpha}\nabla T$, where

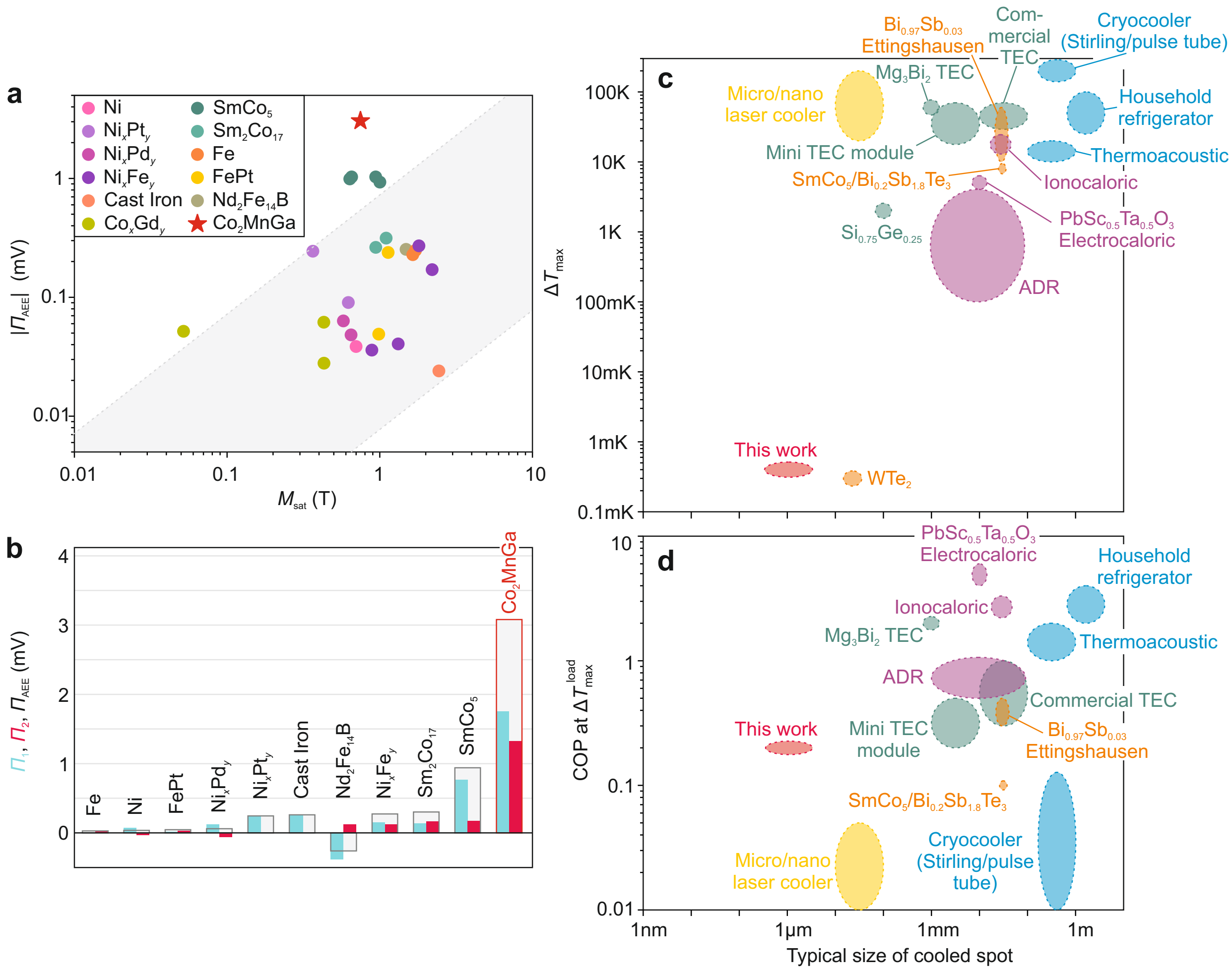

Figure 4: **Comparison of the anomalous Ettingshausen coefficient of Co_2MnGa with literature. a,** Absolute values of anomalous Ettingshausen coefficient as a function of saturation magnetization M_{sat}. 0.5 mm-thick Fe, Ni, $Ni_{95}Pt_5$, $Ni_{75}Pt_{25}$, $Ni_{70}Pd_{30}$, $Ni_{95}Fe_5$, $Ni_{75}Fe_{25}$, $Ni_{50}Fe_{50}$, $Ni_{25}Fe_{75}$ and $Fe_{50}Pt_{50}$,[9] 10 nm-thick FePt,[24] 1 mm-thick ductile and grey cast iron,[8] 30 nm-thick $Co_{86}Gd_{14}$, $Co_{78}Gd_{22}$ and $Co_{58}Gd_{42}$,[25] 1.5 mm-thick $SmCo_5$, Sm_2Co_{17}-type magnet and $Nd_2Fe_{17}B$.[7] **b,** Total anomalous Ettingshausen coefficient Π_{AEE} (grey bars) along with its two contributing components: the intrinsic term Π_1 (blue bars) and the extrinsic term Π_2 (red bars). 10 nm-thick Fe, Ni, $Fe_{50}Pt_{50}$, $Ni_{70}pd_{30}$, $Ni_{75}Pt_{25}$ and $Ni_{50}Fe_{50}$,[9] 1 mm-thick cast iron,[8] 1.5 mm-thick $Nd_2Fe_{17}B$, $SmCo_5$ and Sm_2Co_{17}.[7] **c,** Comparison of the maximum achievable ΔT, and **d,** the coefficient of performance at $\Delta T^{\mathrm{load}}_{\mathrm{max}}$ for coolers of various sizes connected to a thermal load. Blue: Stirling (-analogue) type engines; green: longitudinal thermoelectrics; orange: transverse thermoelectrics; purple: caloric coolers; yellow: optical cooler. Data from: anomalous Ettingshausen WTe_2 cooler,[26] electrocaloric $PbSc_{0.5}Ta_{0.5}O_3$ (COP at $\Delta T \approx 2.5$ K),[27] ionocaloric refrigeration (COP at $\Delta T \approx 15$ K),[28] Mg_3Bi_2-based Peltier cooler (COP at $\Delta T \approx 10$ K),[29] thermoacoustic cooler (COP at $\Delta T \approx 10$ K),[30] $Bi_{0.97}Sb_{0.03}$ Ettingshausen cooler (COP at $\Delta T \approx 20$ K and $B = 1$ T),[31] transverse $SmCo_5/Bi_{0.2}Sb_{1.8}Te_3$ cooler (COP at $\Delta T \approx 8$ K),[32] laser cooling (COP at $\Delta T \approx 50$ K),[33,34] commercial thermoelectric coolers (TEC) (COP at $\Delta T \approx 25$ K), mini TEC module (COP at $\Delta T \approx 30$ K),[35] cryocoolers (COP at $\Delta T \approx 100$ K) and household refrigerator (COP at $\Delta T \approx 25$ K),[36,37] mini TEC BiSbTe module,[38] Bi_2Te_3-based thin film superlattices,[39] $Si_{0.75}Ge_{0.25}$ micro refrigerators,[40] adiabatic demagnetization refrigerator (ADR) (COP at $\Delta T \approx 1$ K).[41]

$\boldsymbol{\sigma}$ and $\boldsymbol{\alpha}$ are the electrical conductivity and thermoelectric tensors, respectively. Under open-circuit conditions ($\mathbf{j}_\mathrm{c} = 0$), the thermopower tensor is given by $\boldsymbol{S} = \boldsymbol{\sigma}^{-1}\boldsymbol{\alpha}$, where the components of $\boldsymbol{S}$ are defined as $S_{ij} = E_i/\nabla_j T$.[21] Expanding this relation in matrix form yields $S_{yx} = (1/\sigma_{xx})(\alpha_{yx} - \sigma_{yx}S_{xx})$, where $S_{xx} = \alpha_{xx}/\sigma_{xx}$. Estimating $\sigma_{xx} \approx 1/\rho_{xx}$ and $\sigma_{xy} \approx \rho_{xy}/\rho_{xx}^2$, where ρ_{ij} denotes the components of the resistivity tensor, we can separate the intrinsic (S_1) and extrinsic (S_2) contributions as

$$S_\mathrm{ANE} = S_1 + S_2 = \rho_{xx}\alpha_{xy} - \rho_{xy}\alpha_{xx}. \tag{5}$$

By Onsager reciprocity, the AEE corresponding expression is

$$\Pi_\mathrm{AEE} = \Pi_1 + \Pi_2 = (\rho_{xx}\alpha_{xy} - \rho_{xy}S_{xx})T. \tag{6}$$

Similar to its Onsager counterpart, the AEE comprises both intrinsic (Π_1) and extrinsic (Π_2) contributions.[7–9,19] The former originates from the off-diagonal thermoelectric tensor component α_{xy}, which directly couples an applied electric current to a transverse temperature gradient. A large α_{xy} indicates a strong Berry curvature contribution, producing an anomalous velocity of charge carriers near the Fermi level that is perpendicular to the applied electric field. The latter contribution arises from the anomalous Hall effect (AHE) acting on the longitudinal current generated by the Seebeck effect.

To estimate such contributions, we performed magnetoresistance and Hall measurements on our Co_2MnGa films (see Supporting Information Figure S9a and b). Using the experimental values of S_xx, Π_AEE, ρ_xx and ρ_xy, we calculate a large transverse thermoelectric coefficient $\alpha_{xy} = 3.73 \pm 1.09$ A $(\mathrm{Km})^{-1}$. This value can be used to estimate Π_1 and Π_2 (see Supporting Information section 6), which we compare to values reported in the literature in Figure 4b. Furthermore, we find that there is a noticeable contribution of 57 ± 8 % from the Berry curvature Π_1 to the overall anomalous Ettingshausen effect, underlining the importance of the intrinsic topological nature of Co_2MnGa to explain the large Π_AEE observed in our experiments.

In the following, we discuss the performance of the Co_2MnGa cooling devices developed in this study. Figure 4c compares the typical maximum cooling ΔT_{max} achieved across various cooling technologies. Among the solid-state cooling approaches suitable for integration into functional devices, the most technologically relevant are electrocaloric (purple) and thermoelectric coolers operating in either the longitudinal (green) or transverse (orange) configuration. As shown, the ΔT_{max} of our micro-scale Co_2MnGa coolers remains smaller than that of most commercial or laboratory-scale coolers.

Longitudinal thermoelectric devices suffer from the need to form complementary p- and n-type pillar structures, requiring precise doping and introducing numerous electrical contacts and thermal interfaces that severely limit efficiency. This limitation can be mitigated by transverse thermoelectrics based on the Ettingshausen effect. Cooling by tens of kelvin has been demonstrated in elemental bismuth and Bi/Sb alloys, but only under large magnetic fields up to 11 T to reach the quantum limit.[1] At the microscale, semimetallic WTe_2 anomalous Ettingshausen coolers have achieved ΔT of up to 0.2 mK, yet again requiring high magnetic fields of approximately 2 T.[26] For practical spot-cooling applications, this reliance on strong external magnetic fields represents a major constraint. In contrast, the absolute anomalous Ettingshausen (AEE) cooling achieved in our Co_2MnGa thin films is larger than the value reported for semimetallic WTe_2, while operating under substantially weaker magnetic field (50 mT). Further design considerations, discussed in the Supporting Information, suggest strategies to extend the operating range of the cooling devices. These include smoothing the junction edges to minimize current crowding at the geometrical Peltier junction and incorporating passive cooling layers on the top side to enhance heat dissipation. Following these strategies, we find that ΔT can be increased to -4 mK.

Ultimately, on-chip applications would benefit from zero-field operation, which could be realized by enhancing the remanent magnetization, engineering the magnetic anisotropy, or employing exchange bias. Several approaches have already been demonstrated to tailor the magnetic configuration in Co_2MnGa: ion irradiation to introduce controlled point defects in the lattice;[42] nanostructure engineering to exploit the interplay between shape and magnetocrystalline anisotropy;[43] and spin–orbit torque in Co_2MnGa/Ta heterostructures, enabling purely electrical control of magnetization.[44] Collectively, these strategies provide a versatile toolbox—spanning both material and device levels—to achieve zero-field thermoelectric functionality.

Lastly, we evaluated the coefficient of performance (COP) of our cooling device. Our analysis employs the thermodynamic framework developed by Herman[1] (see Supporting Information section 10) where the COP is given by:

$$\mathrm{COP} = \frac{j_c \Pi_{AEE} - \frac{1}{2} j_c^2 \rho L - (1 - Z_{ANE}\overline{T})\kappa \frac{\Delta T}{L}}{j_c^2 \rho L + j_c \Pi_{AEE} \frac{\Delta T}{T_\mathrm{c}}} \tag{7}$$

Here, T_c is the temperature of the cooling surface, ρ is the electrical resistivity, L is the device thickness, κ is the thermal conductivity, and $Z_{\mathrm{ANE}} = (\Pi_{\mathrm{AEE}} T_\mathrm{c})^2/(\rho\kappa)$ is the thermomagnetic figure of merit. The average temperature is defined as $\overline{T} = (T_{\mathrm{substrate}} + T_c)/2$, and the temperature difference as $\Delta T = T_{\mathrm{substrate}} - T_c$. The numerator comprises three distinct heat flow contributions. The first term, q_{AEE}, quantifies the heat flux generated by the anomalous Ettingshausen effect. The second term, $q_{\mathrm{Joule}}/2$, accounts for Joule heating directed toward the cold side as only half the total Joule heat contributes since the remainder flows toward the substrate. The third term represents the parasitic thermal conductance from the heat sink ($T_{substrate}$) to the cold side (T_c) through the ribbon of thickness L when a temperature gradient, $\Delta T/L = (T_{substrate} - T_c)/L$ is established. The denominator represents the electrical power input required to sustain the effect. We find a COP of 0.4 at $\Delta T \approx$ 0.4 mK (see Supporting Information section 10). This value is compared to other cooling technologies in Figure 4d.

Conclusion

In summary, we report a giant anomalous Ettingshausen effect in thin films of the magnetic Weyl semimetal Co_2MnGa. By combining scanning thermal microscopy measurements and electrical magnetotransport experiments, we uncovered a substantial intrinsic anomalous Ettingshausen component due to the large Berry curvature near the Fermi energy of Co_2MnGa. This intrinsic contribution, coupled with the extrinsic counterpart, synergistically enhances the overall cooling efficiency. This efficiency is further enhanced by nanostructuring. The geometrically induced local Peltier effect in nm-sized Co_2MnGa nanoribbons adds to the anomalous Ettingshausen effect leading to a boost of cooling performance by 170%. These results highlight the strong influence of non-trivial band topology on transverse thermoelectric effects and underscore the potential for high-efficiency on-chip cooling. Such advances could address critical needs in thermal management, sensing, quantum computing, and healthcare applications such as cold-chain logistics for vaccines.

Methods

Material synthesis and device preparation

Co_2MnGa film growth

Epitaxial deposition of 50 nm Co_2MnGa thin films was carried out using a Kurt J Lesker CMS-18 magnetron sputtering system with a base pressure below 4×10^{-6} Pa (3×10^{-8} Torr) on MgO(001) substrates. Prior to thin film fabrication, substrates were cleaned with Ar plasma and were subsequently annealed at 400 °C for 30 minutes in the vacuum chamber. The deposition of Co_2MnGa thin films was performed by DC magnetron sputtering from a stoichiometric polycrystalline target at 100 W under 0.8 Pa (6 mTorr) of Ar, with a growth rate of 0.8 Ås^{-1} at 400 °C. During the deposition, the sample holder was rotated and post-annealing was conducted in situ at 400 °C for 20 minutes. Following the cooling down to ambient temperature, a 2 nm Ta protective layer was deposited on the top.

Sample Preparation

Hall bars (l = 2000 µm, w = 150 µm) for transport measurements were patterned using photolithography, followed by Ar ion milling. For thermometry measurements, the Co_2MnGa is patterned into U-shaped devices using standard electron beam lithography followed by ion milling. The legs have a length of 20 µm, and a channel width of 1–4 µm. Nanoribbons with a width of 200 nm were formed by further milling the channel using a Ga^{2+} focused ion beam. No extra metals were evaporated and electrical contact to the devices was made by directly wire-bonding to the Co_2MnGa films.

Scanning Thermal Microscopy

Scanning Thermal Microscopy (SThM) was used for both, temperature mapping and thermal conductivity measurements. Measurements were conducted with a Bruker Dimension Icon Atomic Force Microscope (AFM) under ambient conditions using VITA-DM-GLA-1 probes featuring a palladium heater on a silicon nitride cantilever/tip, with a typical tip radius ranging from 25 to 60 nm. We performed a calibration of the tip radius using a method described elsewhere[45,46] and obtained 51 nm. The heater, integrated into a modified Wheatstone bridge, was driven by a combined 91 kHz AC and DC bias, as detailed elsewhere.[14] Detection of the signal was achieved through an SR-830 lock-in amplifier, and the amplitude output was directed to the AFM controller. Thermal maps were generated by calculating $T_{\mathrm{AEE}} = A \cdot \cos\phi$, where A represents the temperature variation amplitude obtained through tip calibration, and ϕ denotes the phase shift. Given the negligible effect of thermal diffusion in our experimental setup (see Supporting Information Section 1), ϕ effectively determines the sign of the temperature variation, indicating whether cooling or heating is occurring.

Temperature measurements

For magnetic field-dependent AC-thermometry measurements, the sample is biased at a frequency of $f = 17$ Hz unless otherwise specified. The SThM tip is driven with $V_{\mathrm{pp}} = 4$ V and $V_{\mathrm{DC}} = 2$ V at a high frequency of $f = 91$ kHz, resulting in a temperature increase of the tip by $\Delta T_{\mathrm{tip}} \approx 7.5$ K. The direct current (DC) signal is recorded using an SRS830 lock-in at the same frequency as the tip excitation. T_{AEE} and T_{Joule} are determined by demodulating the signal using a Zurich Instruments MFLI lock-in amplifier at the 1st and 2nd harmonics while the SThM tip scans over the surface or is held at a constant position. The magnetic field is applied by an home-built electromagnet.

The scan speed is limited by the time to reach i) thermal equilibrium and ii) lock-in signal saturation. We assume that thermal equilibrium is reached after about 1 ms, which corresponds to the thermalization time of the SThM probes used in this experiment. In the lock-in detection scheme presented in this paper we used a time constant (Tc) of 150 ms and 4th filter order. Thus, to reach the (63%) 90% of the final value of the measured signal a time equivalent to (4.4 Tc) 6.7 Tc is required. This corresponds to approximately (660 ms) 1 s. When scanning the surface, we use a scan rate of 1 s (or slower) per pixel. For a 20x20 µm scanning area with 250x250 pixels and 8 nm spatial resolution, this results in a tip speed of 0.08 µmm/s. A faster scan rate significantly attenuates the signal and introduces noise into the maps.

Acknowledgement

P.G., J.S. and V.F. acknowledge financial support from the F.R.S.-FNRS of Belgium (FNRS-CQ-1.C044.21-SMARD, FNRS-CDR-J.0068.21-SMARD, FNRS-MIS-F.4523.22-TopoBrain, FNRS-PDR-T.0128.24-ART-MULTI, FNRS-CR-1.B.463.22-MouleFrits, FNRS-FRIA-1.E092.23-TOTEM, FNRS-GEQ-UG.0102.2F-Attohmics). P.G. acknowledges financial support from the EU (ERC-StG-10104144-MOUNTAIN), from the Federation Wallonie-Bruxelles through the ARC Grant No. 21/26-116, and from the FWO and FRS-FNRS under the Excellence of Science (EOS) programme (40007563-CONNECT). R.J. and L.M.C.P. acknowledge financial support from the KU Leuven.

Author contributions

P.G. conceived and supervised the study. Y.Z. and S.G. grew the Co_2MnGa thin films and performed the magnetotransport measurements. R.J. and L.M.C.P performed the volumetric magnetometry experiments. V.F., Mo.R. and Mi.R. fabricated the U-shaped devices. P.S.D. and J.M.R.W. fabricated the SThM probes. Mo.R., V.F. and J.S. performed the SThM experiments and evaluated the data. Mo.R., J.S. and P.G. wrote the manuscript with input from all co-authors. All authors have given approval to the final version of the manuscript.

ASSOCIATED CONTENT

A preprint version of this work has been deposited on a public repository: Razeghi, M.; Spiece, J.; Fonck, V.; Zhang, Y.; Rohde, M.; Joris, R.; Dobson, P. S.; Weaver, J. M. R.; da Costa Pereira, L.; Granville, S.; Gehring, P. Record-high Anomalous Ettingshausen effect in a micron-sized magnetic Weyl semimetal on-chip cooler. 2024, Article arXiv 2403.13598. arXiv. https://arxiv.org/abs/2403.13598 (accessed November 6, 2025).

Supporting Information Available

The Supporting Information is available free of charge at

- AC lock-in thermometry; Peltier and Magneto-Peltier effects; Joule heating quantification; geometrically induced thermoelectric effects; spatial temperature distributions; magneto-transport and magnetometry measurements; thermal conductivity characterization; COMSOL simulations; and device performance estimations.

- Supplementary Figures. 1–16, sections 1-10.

References

(1) Harman, T.; Honig, J.; Fischler, S.; Paladino, A.; Button, M. J. Oriented single-crystal bismuth Nernst-Ettingshausen refrigerators. *Applied Physics Letters* **1964**, *4*, 77–79.

(2) Reichlova, H.; Schlitz, R.; Beckert, S.; Swekis, P.; Markou, A.; Chen, Y.-C.; Kriegner, D.; Fabretti, S.; Hyeon Park, G.; Niemann, A., et al. Large anomalous Nernst effect in thin films of the Weyl semimetal Co_2MnGa. *Applied Physics Letters* **2018**, *113*, 212405.

(3) Yang, H.; You, W.; Wang, J.; Huang, J.; Xi, C.; Xu, X.; Cao, C.; Tian, M.; Xu, Z.-A.; Dai, J.; Li, Y. Giant anomalous Nernst effect in the magnetic Weyl semimetal $Co_3Sn_2S_2$. *Physical Review Materials* **2020**, *4*, 024202.

(4) Bridgman, P. The connections between the four transverse galvanomagnetic and thermomagnetic phenomena. *Physical Review* **1924**, *24*, 644–651.

(5) Mizuno, H.; Modak, R.; Hirai, T.; Takahagi, A.; Sakuraba, Y.; Iguchi, R.; Uchida, K.-i. Deposition temperature dependence of thermo-spin and magneto-thermoelectric conversion in Co_2MnGa films on $Y_3Fe_5O_{12}$ and $Gd_3Ga_5O_{12}$. *Applied Physics Letters* **2022**, *120*, 202401.

(6) Zhang, Y.; Yin, Y.; Dubuis, G.; Butler, T.; Medhekar, N. V.; Granville, S. Berry curvature origin of the thickness-dependent anomalous Hall effect in a ferromagnetic Weyl semimetal. *npj Quantum Materials* **2021**, *6*, 17.

(7) Miura, A.; Sepehri-Amin, H.; Masuda, K.; Tsuchiura, H.; Miura, Y.; Iguchi, R.; Sakuraba, Y.; Shiomi, J.; Hono, K.; Uchida, K.-i. Observation of anomalous Etting-

shausen effect and large transverse thermoelectric conductivity in permanent magnets. *Applied Physics Letters* **2019**, *115*, 222403.

(8) Nagasawa, R.; Oyanagi, K.; Hirai, T.; Modak, R.; Kobayashi, S.; Uchida, K.-i. Anomalous Ettingshausen effect in iron–carbon alloys. *Applied Physics Letters* **2022**, *121*, 062401.

(9) Miura, A.; Iguchi, R.; Seki, T.; Takanashi, K.; Uchida, K.-i. Spin-mediated charge-to-heat current conversion phenomena in ferromagnetic binary alloys. *Physical Review Materials* **2020**, *4*, 034409.

(10) Uchida, K.-i.; Daimon, S.; Iguchi, R.; Saitoh, E. Observation of anisotropic magneto-Peltier effect in nickel. *Nature* **2018**, *558*, 95–99.

(11) Zolotavin, P.; Evans, C. I.; Natelson, D. Substantial local variation of the Seebeck coefficient in gold nanowires. *Nanoscale* **2017**, *9*, 9160–9166.

(12) Harzheim, A.; Spiece, J.; Evangeli, C.; McCann, E.; Falko, V.; Sheng, Y.; Warner, J. H.; Briggs, G. A. D.; Mol, J. A.; Gehring, P., et al. Geometrically enhanced thermoelectric effects in graphene nanoconstrictions. *Nano Letters* **2018**, *18*, 7719–7725.

(13) Menges, F.; Mensch, P.; Schmid, H.; Riel, H.; Stemmer, A.; Gotsmann, B. Temperature mapping of operating nanoscale devices by scanning probe thermometry. *Nature Communications* **2016**, *7*, 10874.

(14) Spiece, J.; Evangeli, C.; Lulla, K.; Robson, A.; Robinson, B.; Kolosov, O. Improving accuracy of nanothermal measurements via spatially distributed scanning thermal microscope probes. *Journal of Applied Physics* **2018**, *124*, 015101.

(15) Das, R.; Iguchi, R.; Uchida, K.-i. Systematic investigation of anisotropic magneto–peltier effect and anomalous ettingshausen effect in Ni thin films. *Physical Review Applied* **2019**, *11*, 034022.

(16) Miura, A.; Masuda, K.; Hirai, T.; Iguchi, R.; Seki, T.; Miura, Y.; Tsuchiura, H.; Takanashi, K.; Uchida, K.-i. High-temperature dependence of anomalous Ettingshausen effect in $SmCo_5$-type permanent magnets. *Applied Physics Letters* **2020**, *117*, 082408.

(17) Rong, B.; Ren, L.; Liu, Y.; Sun, B.; Chen, J.; Teo, K. L.; Liu, L.; Yang, Y. Evidences of thermoelectrically driven unidirectional magnetoresistance from a single Weyl ferromagnet Co_2MnGa. *Applied Physics Letters* **2023**, *11*, 121109.

(18) Hu, J.; Zhang, Y.; Huo, X.; Li, N.; Liu, S.; Yu, D.; Ansermet, J.-P.; Granville, S.; Yu, H. Large Anomalous Nernst Angle in Co_2MnGa Thin Film. *IEEE Magnetics Letters* **2022**, *13*, 1–5.

(19) Sumida, K.; Sakuraba, Y.; Masuda, K.; Kono, T.; Kakoki, M.; Goto, K.; Zhou, W.; Miyamoto, K.; Miura, Y.; Okuda, T., et al. Spin-polarized Weyl cones and giant anomalous Nernst effect in ferromagnetic Heusler films. *Communications Materials* **2020**, *1*, 89.

(20) Guin, S. N.; Manna, K.; Noky, J.; Watzman, S. J.; Fu, C.; Kumar, N.; Schnelle, W.; Shekhar, C.; Sun, Y.; Gooth, J., et al. Anomalous Nernst effect beyond the magnetization scaling relation in the ferromagnetic Heusler compound Co_2MnGa. *npg Asia Materials* **2019**, *11*, 16.

(21) Xu, L.; Li, X.; Ding, L.; Chen, T.; Sakai, A.; Fauqué, B.; Nakatsuji, S.; Zhu, Z.; Behnia, K. Anomalous transverse response of Co_2MnGa and universality of the room-temperature $\alpha_{ij}^A/\sigma_{ij}^A$ ratio across topological magnets. *Phys. Rev. B* **2020**, *101*, 180404.

(22) Sakai, A.; Mizuta, Y. P.; Nugroho, A. A.; Sihombing, R.; Koretsune, T.; Suzuki, M.-T.; Takemori, N.; Ishii, R.; Nishio-Hamane, D.; Arita, R., et al. Giant anomalous Nernst effect and quantum-critical scaling in a ferromagnetic semimetal. *Nature Physics* **2018**, *14*, 1119–1124.

(23) Behnia, K. The Nernst effect and the boundaries of the Fermi liquid picture. *Journal of Physics: Condensed Matter* **2009**, *21*, 113101.

(24) Seki, T.; Iguchi, R.; Takanashi, K.; Uchida, K. Relationship between anomalous Ettingshausen effect and anomalous Nernst effect in an FePt thin film. *Journal of Physics D: Applied Physics* **2018**, *51*, 254001.

(25) Seki, T.; Miura, A.; Uchida, K.-i.; Kubota, T.; Takanashi, K. Anomalous Ettingshausen effect in ferrimagnetic Co–Gd. *Applied Physics Express* **2019**, *12*, 023006.

(26) Völkl, T.; Aharon-Steinberg, A.; Holder, T.; Alpern, E.; Banu, N.; Pariari, A.; Myasoedov, Y.; Huber, M.; Hücker, M.; Zeldov, E. Demonstration and imaging of cryogenic magneto-thermoelectric cooling in a van der Waals semimetal. *Nature Physics* **2024**, *20*, 976–983.

(27) Wang, Y.; Zhang, Z.; Usui, T.; Benedict, M.; Hirose, S.; Lee, J.; Kalb, J.; Schwartz, D. A high-performance solid-state electrocaloric cooling system. *Science* **2020**, *370*, 129–133.

(28) Lilley, D.; Prasher, R. Ionocaloric refrigeration cycle. *Science* **2022**, *378*, 1344–1348.

(29) Lin, C.; Ma, X.; Liang, K.; Xu, Y.; Yang, H.; Wang, J.; Ye, S.; Qiu, J.; Song, L.; Zhi, S., et al. Miniaturized Mg3Bi2-based thermoelectric cooler for localized electronic thermal management. *Nature Communications* **2025**, *16*, 7779.

(30) Remiorz, L.; Grzywnowicz, K.; Remiorz, E.; Uchman, W. Designing a Thermoacoustic Cooler for Energy Applications: Experimental Insights. *Energies* **2025**, *18*.

(31) Hawkins, S. R.; Kooi, C. F.; Cuff, K. F.; Weaver, J. L.; Horst, R. B.; Enslow, G. M. Low-Temperature Ettingshausen Coolers, Advances in Cryogenic Engineering, Springer US, 1964.

(32) Murata, M.; Ando, F.; Hirai, T.; Adachi, H.; ichi Uchida, K. Quantitative measurements of transverse thermoelectric generation and cooling performances in SmCo5/Bi0.2Sb1.8Te3-based artificially tilted multilayer module. *Science and Technology of Advanced Materials* **2025**, *26*, 2535955.

(33) Rayner, A.; Heckenberg, N. R.; Rubinsztein-Dunlop, H. Condensed-phase optical refrigeration. *J. Opt. Soc. Am. B* **2003**, *20*, 1037–1053.

(34) Pant, A.; Xia, X.; Davis, E. J.; Pauzauskie, P. J. Solid-state laser refrigeration of a composite semiconductor Yb: YLiF4 optomechanical resonator. *Nature communications* **2020**, *11*, 3235.

(35) Zhang, Y.; Christofferson, J.; Shakouri, A.; Zeng, G.; Bowers, J.; Croke, E. On-chip high speed localized cooling using superlattice microrefrigerators. *IEEE Transactions on Components and Packaging Technologies* **2006**, *29*, 395–401.

(36) Lee, H. *Thermal Design*; John Wiley & Sons, Ltd, 2022; Chapter 5, pp 335–508.

(37) Shakouri, A.; Zebarjadi, M. In *Thermal Nanosystems and Nanomaterials*; Volz, S., Ed.; Springer Berlin Heidelberg: Berlin, Heidelberg, 2009; pp 225–299.

(38) Qiu, J.; Yan, Y.; Luo, T.; Tang, K.; Yao, L.; Zhang, J.; Zhang, M.; Su, X.; Tan, G.; Xie, H.; Kanatzidis, M. G.; Uher, C.; Tang, X. 3D Printing of highly textured bulk thermoelectric materials: mechanically robust BiSbTe alloys with superior performance. *Energy Environ. Sci.* **2019**, *12*, 3106–3117.

(39) Chowdhury, I.; Prasher, R.; Lofgreen, K.; Chrysler, G.; Narasimhan, S.; Mahajan, R.; Koester, D.; Alley, R.; Venkatasubramanian, R. On-chip cooling by superlattice-based thin-film thermoelectrics. *Nature nanotechnology* **2009**, *4*, 235–238.

(40) Zhang, Y.; Christofferson, J.; Shakouri, A.; Zeng, G.; Bowers, J.; Croke, E. On-chip

high speed localized cooling using superlattice microrefrigerators. *IEEE Transactions on Components and Packaging Technologies* **2006**, *29*, 395–401.

(41) Fernandes, C.; Almeida, R.; Amaral, J.; Belo, J.; Ventura, J.; Silva, D. Solid-state magnetic refrigerator based on the demagnetizing effect. *International Journal of Refrigeration* **2025**, *178*, 272–279.

(42) Mahendra, A.; Murmu, P. P.; Acharya, S. K.; Islam, A.; Fiedler, H.; Gupta, P.; Granville, S.; Kennedy, J. Shaping Perpendicular Magnetic Anisotropy of Co2MnGa Heusler Alloy Using Ion Irradiation for Magnetic Sensor Applications. *Sensors* **2023**, *23*, 4564.

(43) Finizio, S.; Kronenberg, A.; Vafaee, M.; Foerster, M.; Litzius, K.; Lucia, A. d.; Menteş, T. O.; Aballe, L.; Krüger, B.; Jourdan, M.; Kläui, M. Magnetic configurations in nanostructured Co2MnGa thin film elements. *New Journal of Physics* **2015**, *17*, 083030.

(44) Ren, L.; Liu, L.; Song, X.; Zhao, T.; Xing, X.; Feng, Y. P.; Chen, J.; Teo, K. L. Manipulation of the Topological Ferromagnetic State in a Weyl Semimetal by Spin–Orbit Torque. *Nano Letters* **2023**, *23*, 3394–3400.

(45) Spièce, J.; Evangeli, C.; Robson, A. J.; El Sachat, A.; Haenel, L.; Alonso, M. I.; Garriga, M.; Robinson, B. J.; Oehme, M.; Schulze, J., et al. Quantifying thermal transport in buried semiconductor nanostructures via cross-sectional scanning thermal microscopy. *Nanoscale* **2021**, *13*, 10829–10836.

(46) Gonzalez-Munoz, S.; Agarwal, K.; Castanon, E. G.; Kudrynskyi, Z. R.; Kovalyuk, Z. D.; Spièce, J.; Kazakova, O.; Patanè, A.; Kolosov, O. V. Direct Measurements of Anisotropic Thermal Transport in γ-InSe Nanolayers via Cross-Sectional Scanning Thermal Microscopy. *Advanced Materials Interfaces* **2023**, 2300081.

TOC Graphic

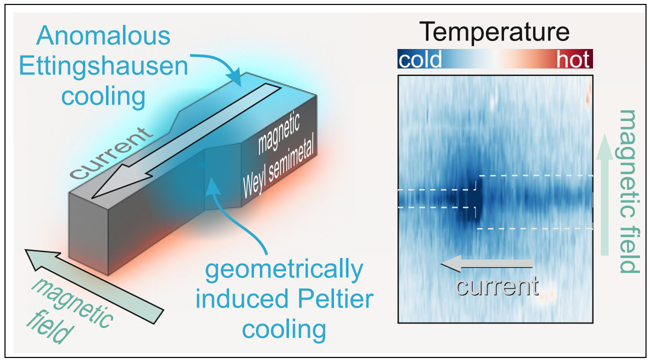
Anomalous
Ettingshausen
cooling
current
magnetic
Weyl semimetal
magnetic
field
geometrically
induced Peltier
cooling
Temperature
cold
hot
current
magnetic field